Supplementary Material:
Digitized counterdiabatic quantum critical dynamics

Anne-Maria Visuri,[1,*] Alejandro Gomez Cadavid,[1,2] Balaganchi A. Bhargava,[1]
Sebastián V. Romero,[1,2] András Grabarits,[3] Pranav Chandarana,[1,2]
Enrique Solano,[1,†] Adolfo del Campo,[3,4,‡] and Narendra N. Hegade[1,§]

[1] *Kipu Quantum GmbH, Greifswalderstrasse 212, 10405 Berlin, Germany*
[2] *Department of Physical Chemistry, University of the Basque Country UPV/EHU, Apartado 644, 48080 Bilbao, Spain*
[3] *Department of Physics and Materials Science, University of Luxembourg, L-1511 Luxembourg, Luxembourg*
[4] *Donostia International Physics Center, E-20018 San Sebastian, Spain*

In this Supplementary Information, we provide further notes and extended results to support and elucidate the findings in the main text. We describe in detail how our experiments were conducted on IBM and discuss the impact of different sources of error that might cause deviations from the expected results. We describe the derivation of the first-order nested commutator expansion of the adiabatic gauge potential for the transverse-field Ising model. We also provide a step-by-step derivation of the cumulants of the defect number distribution in the fast-quench limit. Finally, for completeness, we discuss the time evolution of the cumulants, which in the main text are only shown at the final time.

CONTENTS

I. Digital quantum simulation on IBM hardware 1

II. Implementation errors 2
  A. Trotter errors 2
  B. Hardware errors 4

III. First-order nested commutator calculation 4

IV. Analytical results for fast quenches in the 1D chain 5
  A. Quench without CD 5
  B. Quench with first-order CD expansion 6
    1. Variational coefficient of the first-order CD term 6
    2. Solution of the time-dependent Schrödinger equation 7

V. Cumulants as functions of instantaneous time 8

References 9

I. DIGITAL QUANTUM SIMULATION ON IBM HARDWARE

An important aspect of preparing and running quantum circuits on hardware is to transpile the required quantum operations according to the corresponding native gate sets provided by the platform. These typically consist of a universal gate set that contains several one-qubit gates and a single two-qubit entangling gate. In our experiments, we used the IBM_FEZ and IBM_MARRAKESH platforms, gate-based quantum computers composed of 156 superconducting qubits under a heavy-hexagonal coupling map. Their native gate set is composed of

$$X = \begin{pmatrix} 0 & 1 \\ 1 & 0 \end{pmatrix}, \; \sqrt{X} = \frac{1}{2}\begin{pmatrix} 1+i & 1-i \\ 1-i & 1+i \end{pmatrix}, \; R_z(\theta) = e^{-i\theta Z/2}, \tag{S1}$$

---

[*] anne-maria.visuri@gmail.com
[†] enr.solano@gmail.com
[‡] adolfo.delcampo@uni.lu
[§] narendrahegade5@gmail.com

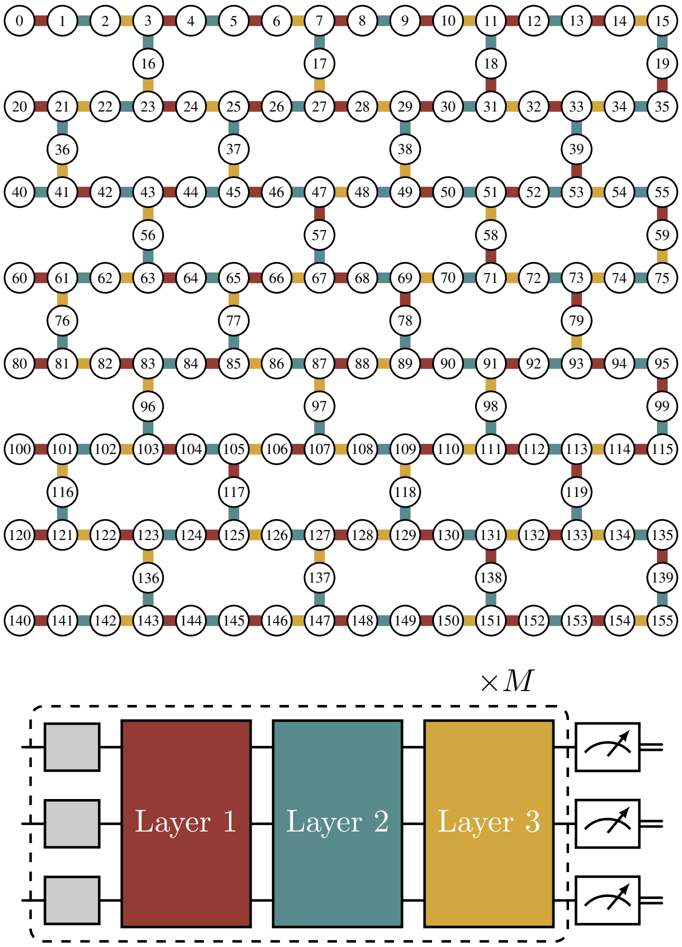

FIG. S1. **Schematic of the IBM_FEZ and IBM_MARRAKESH 156-qubit coupling maps.** Three depth-one layers suffice to realize the two-body interactions between all neighbor pairs for simulating the heavy-hexagonal lattice, finding an optimal circuit decomposition for each Trotter step.

with CZ $= \mathrm{diag}(1,1,1,-1)$ as an entangling gate. In addition to them, IBM has recently introduced the fractional gates $R_{zz}(\theta) = e^{-i\theta Z_0 Z_1/2}$ (with $0 < \theta \leq \pi/2$) and $R_x(\theta) = e^{-i\theta X/2}$ [S1] in their Heron-based processors.

To mitigate the impact of errors coming from noisy hardware on our results, we employed the *as-late-as-possible* scheduling method as an error suppression technique. It strategically introduces delays in the circuit to maximize the time that each qubit remains in its ground state, which may help improve the outcome fidelity. For the heavy-hexagonal lattice, an optimal circuit decomposition can be found relying on the graph coloring theorem. In particular, for each Trotter step, it is possible to reduce all the two-body terms coming from equations (2) and (4) in the main text into a depth-three block using the circuit decomposition shown in Fig. S1.

II. IMPLEMENTATION ERRORS

A. Trotter errors

In this section, we analyze various sources of error that can lead to deviations between experimental results and expected outcomes. First, let us consider the Trotter error. We implement a first-order Trotter decomposition of the continuous evolution governed by $\mathcal{H}(\lambda) = H(\lambda) + \dot{\lambda} A_\lambda$. For each Trotter step $m = 0, \ldots, M$, the quantum circuits realize a product of the two unitaries

$$U_{ad}^m(\delta t) = U_f^m(\delta t) U_i^m(\delta t), \tag{S2}$$

$$U_{cd}^m(\delta t) = e^{-i\delta t/T\cdot 2gJ\alpha_1(\lambda_m)\sum_{\langle i,j\rangle}\hat{Y}_i\hat{Z}_j} e^{-i\delta t/T\cdot 2gJ\alpha_1(\lambda_m)\sum_{\langle i,j\rangle}\hat{Z}_i\hat{Y}_j}. \tag{S3}$$

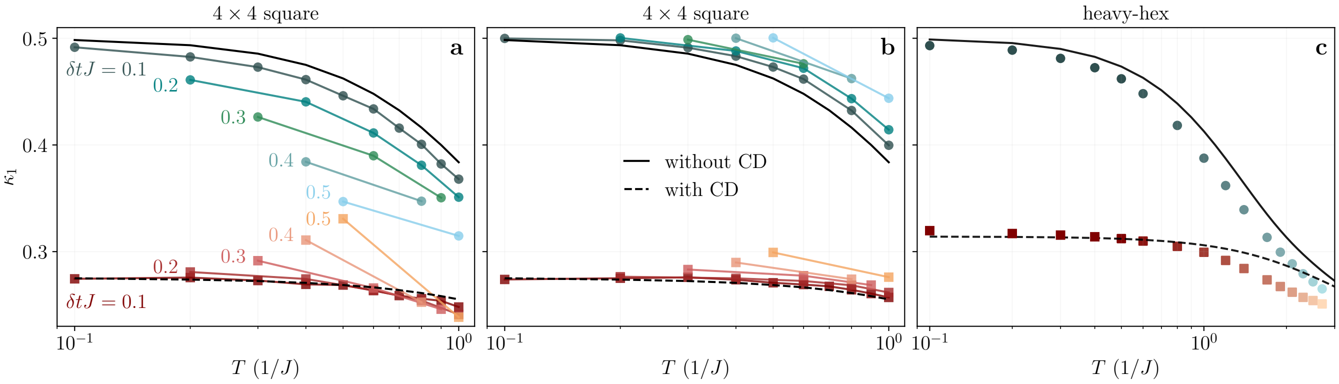

FIG. S2. **Mean density of defects measured at the final evolution time, with and without CD, obtained by MPS simulations of the quantum circuits with MIMIQ [S2].** The colored markers denote the circuit simulations that contain Trotter errors, while the solid and dashed black lines show reference MPS simulations of the time evolution with negligible errors. For a square lattice of size 4 × 4, we simulate a circuit with different Trotter decompositions: **a,** $U_{ad}^m = U_f^m U_i^m$ and **b,** $U_{ad} = U_i^m U_f^m$. In both, U_{cd}^m is given by equation (S3). We use varying time steps $\delta t = 0.1/J, 0.2/J, \ldots, 0.5/J$ as indicated by the color gradients. The blue-shaded circles correspond to the circuits without CD and the red-shaded squares to those with CD. **c,** The markers show the circuit simulation results for a 156-qubit heavy-hexagonal lattice with the decomposition $U_{ad}^m = U_f^m U_i^m$, corresponding to Fig. 3b in the main text. The time step is varied here in the same way as in Fig. 3b: $\delta t = 0.1/J$ for the data points up to $T = 0.5/J$ and for larger T, the number of steps is fixed to 5 so that δt increases. The deviations from the reference solution due to Trotter errors accumulate with increasing T.

Here, $\lambda_m = m\delta t$, $\dot{\lambda} = 1/T$,

$$U_i^m(\delta t) = e^{-i\delta t\cdot(1-\lambda_m)H_i}, \qquad U_f^m(\delta t) = e^{-i\delta t\cdot\lambda_m H_f}, \tag{S4}$$

and the initial and final Hamiltonians are $H_i = -g\sum_i \hat{X}_i$, and $H_f = -J\sum_{\langle i,j\rangle} \hat{Z}_i\hat{Z}_j$. The operators $U_{ad}^m(\delta t)$ and $U_{cd}^m(\delta t)$ correspond to digitized annealing and the counterdiabatic (CD) term, respectively. To assess the errors introduced by the first-order Trotter decomposition, we analyze the mean defect density κ_1 in a square lattice of size 4×4 as a representative case. Figure S2 shows κ_1 as a function of the total evolution time for various values of the time step δt. The data indicated by the markers is obtained via matrix product state (MPS) simulations of the quantum circuit implementing the digitized time evolution, performed with the MIMIQ simulator [S2]. As a reference, Fig. S2 shows the results of MPS simulations using the time-dependent variational principle (TDVP) [S3, S4], with $\delta t = 0.002$, a truncation cutoff of 10^{-20}, and a maximum bond dimension of $\chi = 200$, for which κ_1 is converged within an accuracy given by the linewidth in the plot.

Figure S2 illustrates how the Trotter errors in the quantum circuits lead to deviations in the defect density with respect to the reference values. Although the scaling of the Trotter error with δt is independent of the order in which the terms within each time step are applied, the magnitude and sign of the deviations may depend on this ordering (see also Fig. 1c of the main text). In Fig. S2a, we use the decomposition $U_{ad}^m = U_f^m U_i^m$ to implement the digitized annealing term, while in Fig. S2b, we use the opposite order $U_{ad}^m = U_i^m U_f^m$. We set U_{cd}^m as in equation (S3) in both cases. We find that the magnitude and sign of the deviations differ significantly in these two cases: For digitized annealing without CD (blue-shaded circles), the Trotter errors lead to a reduction of the mean defect density in Fig. S2a whereas in Fig. S2b, they lead to an increase with respect to the reference solution. For the counterdiabatic evolution (red-shaded squares), in panel a, the deviations occur in either direction depending on δt. In panel b, on the other hand, the deviations are only towards larger defect densities, and the magnitude of the deviations is smaller than in panel a. These differences have consequences for the experimental data reported in Fig. 3 of the main text: The Trotter decomposition $U_{ad}^m = U_f^m U_i^m$ is used in all data sets other than the digitized annealing results in Figs. 3c and d, where we instead use $U_{ad}^m = U_i^m U_f^m$. We observe that the small deviations of κ_1 from the reference solution are toward larger values in these experiments, while in Figs. 3b, the experimental κ_1 obtained by digitized annealing is slightly below the reference line for $T \lesssim 2/J$. For the CD evolution, we only observe deviations towards larger defect densities.

In all cases, the circuit simulation results approach the reference lines for decreasing δt. However, increasing δt leads to a reduction in the depth of the circuit, since fewer unitary operations are required in the decompositions given by equations (S3)–(S4). This reduction is advantageous for experimental implementations, as it significantly mitigates gate errors. Thus, determining an optimal δt is crucial to effectively balance Trotter errors and gate errors. In Figs. 3c and d of the main text, this balance is carried out using larger δt values in larger T. This reduces gate errors, but may be a key factor that contributes to the observed increase in the mean defect density as T increases.

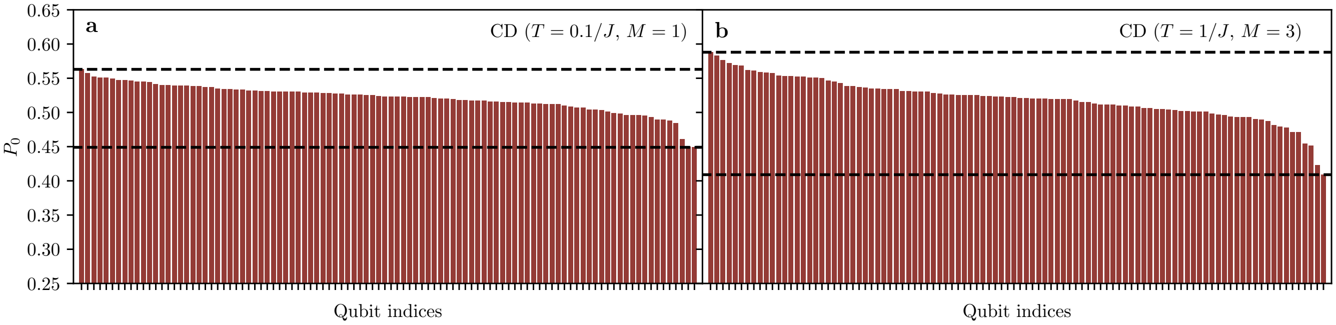

FIG. S3. **Probability per qubit of getting a zero after sampling 20000 times the CD-assisted 100-qubit linear chain. a,** Results using $T = 0.1/J$ (one Trotter step). **b,** Results using $T = 1/J$ (three Trotter steps). For both plots, qubit indices are sorted from largest to smallest P_0 values and dashed lines indicate the maximum and minimum values of P_0.

We also simulate the quantum circuit implementing the time evolution of the heavy-hexagonal lattice, using the same Trotter steps as in Fig. 3b of the main text, to quantify the Trotter error present in the quantum simulation. The data from a MIMIQ simulation of the quantum circuit is shown in Fig. S2c together with the MPS reference solution, which is the same as in Fig. 3b. The deviations due to the Trotter error increase as T increases as expected. The results in Fig. S2 suggest that the systematic shift observed in the experimental data for CD evolution, seen in Fig. 3 of the main text, is not primarily caused by Trotter errors at small T but rather stems from hardware noise. Furthermore, it is important to note that deviations arising from Trotter errors and hardware noise may shift the results in opposite directions, potentially leading to a partial cancellation of errors.

B. Hardware errors

Another significant source of error in our results arises from the platform itself, due to gate and measurement errors, short coherence times of the qubits, and other factors. Their impact can be quantified by studying the probability of measuring a zero as an outcome, P_0, among all samples taken in our experiments. While for an ideal circuit implementation, we would expect a uniform distribution, where the probability of getting either a zero or a one is equal, qubits with shorter coherence times and bit-flip errors may return different results. In Fig. S3, we perform this study for the CD-assisted evolution of a 100-qubit linear chain at times $T = 0.1/J$ (one Trotter step) and $T = 1/J$ (three Trotter steps), corresponding to results in Figs. 2a and 3a of the main text. It can be clearly seen that for three Trotter steps, with a larger circuit depth and a larger number of gates, the probability distribution is further from the ideal uniform distribution in comparison to a single step.

III. FIRST-ORDER NESTED COMMUTATOR CALCULATION

The adiabatic gauge potential (AGP) satisfies the equation $[\partial_\lambda H + i[A_\lambda, H], H] = 0$. Solving this equation has been shown to be equivalent to minimizing the action $S_\lambda(A_\lambda) = \mathrm{Tr}\left(G_\lambda^\dagger G_\lambda\right)$, where G_λ is the conserved operator

$$G_\lambda = \partial_\lambda H + i[A_\lambda, H]. \tag{S5}$$

This minimization can be performed within a limited subset of operators chosen from the Krylov space obtained by repeatedly applying the Liouvillian $\mathcal{L} = [H, \cdot]$ onto $\partial_\lambda H$ [S5], resulting in the ansatz of equation (3) in the main text.

To solve the first-order nested commutator expression for the AGP, we define the operators

$$\hat{O}_0 = \partial_\lambda H, \quad \hat{O}_1 = [H, \hat{O}_0], \quad \hat{O}_2 = [H, \hat{O}_1]. \tag{S6}$$

The first-order AGP is then expressed as $A^1_\lambda = i\alpha_1(\lambda)\hat{O}_1$. We use a variational method to find the coefficient $\alpha_1 \in \mathbb{R}$: We minimize the action $S_\lambda\left(A^1_\lambda\right) = S_1 = \mathrm{Tr}\left(G_1^\dagger G_1\right)$ [S6], where $G_1 = \partial_\lambda H + i[A^1_\lambda, H] = \hat{O}_0 + \alpha_1\hat{O}_2$. The minimization condition requires

$$\frac{\delta S_1}{\delta \alpha_1} = 2\,\mathrm{Tr}\left(\hat{O}_1^\dagger \hat{O}_1\right) + 2\alpha_1\,\mathrm{Tr}\left(\hat{O}_2^\dagger \hat{O}_2\right) = 0, \tag{S7}$$

which implies

$$\alpha_1 = -\frac{\mathrm{Tr}\left(\hat{O}_1^\dagger \hat{O}_1\right)}{\mathrm{Tr}\left(\hat{O}_2^\dagger \hat{O}_2\right)}. \tag{S8}$$

We can now evaluate α_1 for the TFIM. For the Hamiltonian

$$H(\lambda) = -\left(1-\lambda(t)\right) g \sum_{j=1}^{N} \hat{X}_j - \lambda(t) J \sum_{\langle i,j\rangle} \hat{Z}_i \hat{Z}_j, \tag{S9}$$

we have

$$\hat{O}_0 = g \sum_{j=1}^{N} \hat{X}_j - J \sum_{\langle i,j\rangle} \hat{Z}_i \hat{Z}_i, \qquad \hat{O}_1 = -2igJ \sum_{\langle i,j\rangle} \hat{Y}_i \hat{Z}_j, \tag{S10}$$

from which we compute $\hat{O}_2$ and obtain the AGP as

$$A_\lambda^1 = 2gJ\alpha_1(\lambda) \sum_{\langle i,j\rangle} \left(\hat{Y}_i \hat{Z}_j + \hat{Y}_j \hat{Z}_i\right). \tag{S11}$$

When equation (S8) is evaluated for a one-dimensional chain of length N, with open boundary conditions, we get

$$\alpha_1(\lambda) = -\frac{(N-1)}{16g^2(N-1)(\lambda-1)^2 + 4J^2[4(N-1)-3]\lambda^2}. \tag{S12}$$

A general formula for α_1 is found in equation (S20) of ref. [S7], and results in more complicated expressions that we use for the two-dimensional geometries.

IV. ANALYTICAL RESULTS FOR FAST QUENCHES IN THE 1D CHAIN

In this section, we provide an exact solution of the cumulants of the number of defects in the 1D transverse-field Ising model. This extension of ref. [S8] from the Kibble-Zurek regime to sudden quenches is discussed in ref. [S9] for finite-time annealing, while the derivation in the case of counterdiabatic dynamics has not been presented in previous literature.

A. Quench without CD

We obtain the solution of the 1D transverse-field Ising model for periodic boundary conditions. We verify, by computing the cumulants numerically using MPS, that the difference due to open boundary conditions is negligible for the system size considered here. Following a Jordan-Wigner transformation to the free-fermion basis (see refs. [S10, S11] for a derivation), the Hamiltonian $H(\lambda)$ of equation (1) in the main text is expressed as the direct sum of independent two-level systems (TLSs),

$$H(\lambda) = \sum_{k>0} \hat{\psi}_k^\dagger H_k \hat{\psi}_k, \tag{S13}$$

where

$$H_k = 2\left[(1-\lambda)g - \lambda J \cos(ka)\right] Z + 2\lambda J \sin(ka)\, X, \tag{S14}$$

and $\lambda = \lambda(t) = t/T$ is the linear scheduling function. In the following, we set the lattice spacing to $a = 1$. The operator $\hat{\psi}_k := (\hat{c}_k, \hat{c}_{-k}^\dagger)^T$ is a vector of the annihilation $\hat{c}_k$ and creation $\hat{c}_{-k}^\dagger$ operators for fermions of quasimomentum $\pm k$, where $k = \frac{\pi}{N}, \frac{3\pi}{N}, \ldots, \left(\pi - \frac{\pi}{N}\right)$. These momenta correspond to the subspace with an even number of fermions, which is consistent with the initial state for even N. We denote the Pauli matrices by X, Y, Z. The cumulants are obtained from the time-evolved wave function at the end of the process at $t = T$.

The time evolution of the free-fermion system can be solved for each momentum state independently so that it decomposes into the time evolutions of independent TLSs [S12]:

$$i\partial_t \begin{pmatrix} \varphi_1 \\ \varphi_2 \end{pmatrix} = H_k \begin{pmatrix} \varphi_1 \\ \varphi_2 \end{pmatrix}. \tag{S15}$$

Momentum indices are omitted here for brevity. The initial state, ground state of the initial Hamiltonian [equation (1)], is given by $\varphi_1 = 0$ and $|\varphi_2| = 1$. With the time-evolved components, one can express the excitation probabilities within each TLS by projecting the time-evolved states onto the excited state of the final Hamiltonian,

$$H_k(T) = 2J \begin{pmatrix} -\cos k & \sin k \\ \sin k & \cos k \end{pmatrix}, \quad |\mathrm{ES}(T)\rangle = \begin{pmatrix} \sin\frac{k}{2} \\ \cos\frac{k}{2} \end{pmatrix}. \tag{S16}$$

Thus, the excitation probability of the k-th state is given by

$$p_k = \left| \sin\frac{k}{2}\,\varphi_1(T) + \cos\frac{k}{2}\,\varphi_2(T) \right|^2. \tag{S17}$$

The statistics of the defect formation can be described in terms of independent Bernoulli trials [S8, S13], where a defect is formed in momentum state k with probability p_k. This probability equals the expectation value of the number of defects $\kappa_{1,k}$ in momentum state k. The expected total number of defects is therefore given by the sum of all probabilities, $\kappa_1 = \sum_k \kappa_{1,k} = \sum_k p_k$. The cumulants satisfy the recursion relation

$$\kappa_{q,k} = p_k(1-p_k)\frac{d\kappa_{q,k}}{dp_k}. \tag{S18}$$

Taking the limit $\sum_{k>0} f_k \to \frac{1}{\Omega_k}\int_0^\pi f(k)dk$, where $\Omega_k = \pi/N$, we find the cumulants of the defect number distribution as

$$\kappa_1 = \frac{N}{\pi}\int_0^\pi \mathrm{d}k\, p_k, \tag{S19}$$

$$\kappa_2 = \frac{N}{\pi}\int_0^\pi \mathrm{d}k\, p_k(1-p_k), \tag{S20}$$

$$\kappa_3 = \frac{N}{\pi}\int_0^\pi \mathrm{d}k\, p_k(1-p_k)(1-2p_k). \tag{S21}$$

We solve the cumulants as functions of the total quench time T by integrating numerically Eqs. (S19)–(S21).

For fast quenches, the leading-order behavior is captured by the sudden quench limit $T \to 0$, in which the final state is identical to the initial one up to a phase factor, leading to the excitation probability

$$p_k = \cos^2\frac{k}{2}. \tag{S22}$$

Substituting this into Eqs. (S19)–(S21) produces the simple expressions $\kappa_1 = N/2$, $\kappa_2 = N/4$, and $\kappa_3 = 0$ for the sudden-quench cumulants. The number of defects is connected to the defect density as $\hat{N}_{\mathrm{def}} = N\hat{n}_{\mathrm{def}}$, and we obtain the cumulants of the defect density distribution by dividing Eqs. (S19)–(S21) by N. With periodic boundary conditions, N is equal to the number of edges N_e introduced in the main text.

B. Quench with first-order CD expansion

1. *Variational coefficient of the first-order CD term*

In this section, we derive the fast-quench plateau values for the first three cumulants in the presence of the first-order variational CD. We first derive the expression for the variational coefficient α_1 for periodic boundary conditions using the TLS representation. To obtain $A^1_\lambda = i\alpha_1(\lambda)O_1$ in this representation, we express the commutators O_1 and O_2 as the direct sums of the commutators of each TLS Hamiltonian. With H_k defined in equation (S14),

$$O_{0k} = \partial_\lambda H_k = -2(g + J\cos(k))Z + 2J\sin(k)X \tag{S23}$$

$$O_{1k} = [H_k, O_{0k}] = 8igJ\sin(k)\,Y, \tag{S24}$$

$$O_{2k} = [H_k, O_{1k}] = 32gJ\sin(k)\left[((1-\lambda)g - \lambda J\cos(k))X - \lambda J\sin(k)Z\right], \tag{S25}$$

where we have exploited the commutation relations of the Pauli matrices. The action S_1 also decomposes into the sum of the TLS actions, $S_1 = \sum_k S_k = \sum_k \mathrm{Tr}\left(G_k^\dagger G_k\right)$ with $G_k(\lambda) = O_{0k} + \alpha_1(\lambda)$. Exploiting the trace identity for the product of Pauli matrices $\mathrm{Tr}\,(AB) = 2\delta_{AB}$, where $A, B = X, Y, Z$, the total action can be written in the continuum approximation as

$$\begin{aligned}\frac{S_1}{128} &\approx 16\alpha_1^2 g^2 J^2 \frac{N}{\pi}\int_0^\pi \mathrm{d}k\,\sin^2 k\left[\lambda^2 J^2 + (1-\lambda)^2 g^2 - 2\lambda(1-\lambda)Jg\cos k\right] + 2\alpha_1 g^2 J^2 \frac{N}{\pi}\int_0^\pi \mathrm{d}k\,\sin^2 k + C \\ &= 8N\alpha_1^2 g^2 J^2\left[\lambda^2 J^2 + (1-\lambda)^2 g^2\right] + N\alpha_1 g^2 J^2 + C\end{aligned} \tag{S26}$$

where C is a constant independent of α_1. As a result, the minimization $\delta S_1/\delta\alpha_1(\lambda) = 0$ gives

$$\alpha_1(\lambda) = -\frac{1}{16[\lambda^2 J^2 + (1-\lambda)^2 g^2]}. \tag{S27}$$

From this, the CD Hamiltonian reads $H^{\mathrm{CD}} = \sum_{k>0} \hat{\psi}_k^\dagger H_k^{\mathrm{CD}}\,\hat{\psi}_k$, where $H_k^{\mathrm{CD}} = i\dot{\lambda}\alpha_1(\lambda)O_{1k} = h_k Y$ and

$$h_k = \frac{\dot{\lambda}\,gJ\sin k}{2\left[\lambda^2 J^2 + (1-\lambda)^2 g^2\right]}. \tag{S28}$$

2. Solution of the time-dependent Schrödinger equation

Within the sudden quench approximation $T \to 0$, the time evolution is dominated solely by the first-order variational CD term as it is proportional to $1/T$. Thus, the time-dependent Schrödinger equation for a given k-th TLS reads

$$i\partial_t \begin{pmatrix}\varphi_1\\ \varphi_2\end{pmatrix} = (H_k + h_k Y)\begin{pmatrix}\varphi_1\\ \varphi_2\end{pmatrix} \approx h_k Y \begin{pmatrix}\varphi_1\\ \varphi_2\end{pmatrix}. \tag{S29}$$

To compute the exact results in Figs. 2a and 3a of the main text, we integrate this equation numerically using the full Hamiltonian $H_k + h_k Y$. To obtain analytic expressions in the sudden-quench limit $T \to 0$, we neglect the term H_k in the last step. Due to the fact that the time dependence appears only as an overall multiplying factor, an exact solution can be obtained by taking the exponential of the integral of $h_k(t)\,Y$. By exploiting the relations $(Y)^{2n} = \mathbb{I}_2$ and $(Y)^{2n+1} = Y$, the time-evolved state reads

$$\begin{pmatrix}\varphi_1(T)\\ \varphi_2(T)\end{pmatrix} = e^{-i\int_0^T \mathrm{d}t' h_k(t') Y}\begin{pmatrix}0\\ 1\end{pmatrix} = \left[\cos\left(\int_0^T \mathrm{d}t' h_k(t')\right) - i\sin\left(\int_0^T \mathrm{d}t' h_k(t')\right)Y\right]\begin{pmatrix}0\\ 1\end{pmatrix} = \begin{pmatrix}-\sin\left(\int_0^T \mathrm{d}t' h_k(t')\right)\\ \cos\left(\int_0^T \mathrm{d}t' h_k(t')\right)\end{pmatrix}. \tag{S30}$$

Note that due to the derivative $\dot{\lambda}$, we can make a change of variables in the integration,

$$\int_0^T \mathrm{d}t'\,h_k(t') = \int_0^1 \mathrm{d}\lambda\,\frac{1}{2\left[\lambda^2 J^2 + (\lambda-1)^2 g^2\right]}\sin k = \frac{\pi}{4}\sin k, \tag{S31}$$

where we have set $g = J = 1$ for simplicity but the results can be straightforwardly generalized to $g \neq 1$, $J \neq 1$. We find the final state as

$$\begin{pmatrix}\varphi_1(T)\\ \varphi_2(T)\end{pmatrix} = \begin{pmatrix}-\sin\left(\frac{\pi}{4}\sin k\right)\\ \cos\left(\frac{\pi}{4}\sin k\right)\end{pmatrix}. \tag{S32}$$

Knowing the final amplitudes, the excitation probabilities can be expressed as

$$p_k \approx \left|\sin\frac{k}{2}\varphi_1(T) + \cos\frac{k}{2}\varphi_2(T)\right|^2 \approx \cos^2\frac{k}{2}\cos^2\left(\frac{\pi}{4}\sin k\right) + \sin^2\frac{k}{2}\sin^2\left(\frac{\pi}{4}\sin k\right) - \frac{1}{2}\sin k\sin\left(\frac{\pi}{2}\sin k\right). \tag{S33}$$

The sudden-quench approximation, made above in equation (S29), now results in the cumulants $\kappa_1 \approx 0.22N$, $\kappa_2 \approx 0.14N$, and $\kappa_3 \approx 0.04N$.

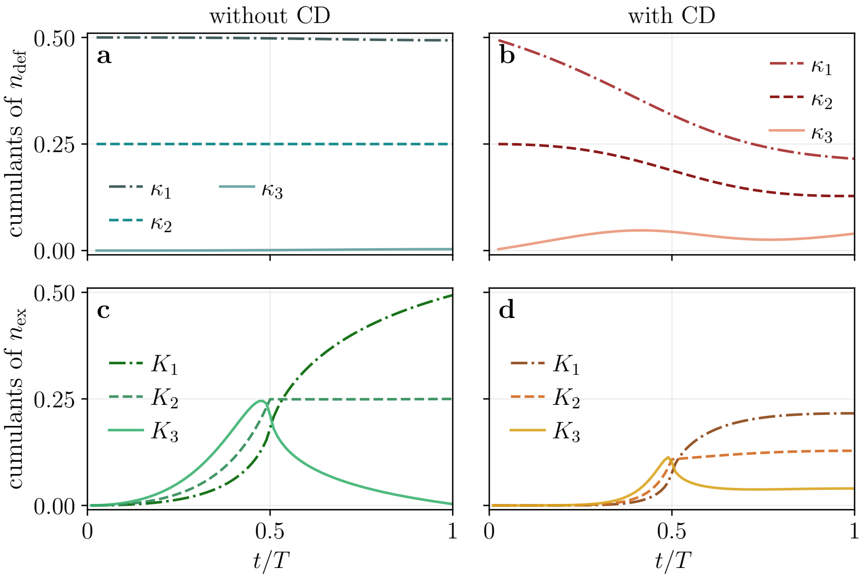

FIG. S4. **The three first cumulants of the distribution of a, b, kinks and c, d, excitations as functions of the unitless time** t/T**.** Here, we consider a one-dimensional lattice of length $N = 100$ and set $T = 0.2/J$. **a, b** The kink density cumulants defined in position basis, given by Eqs. (S34) and (S35), differ from **c, d,** the cumulants of the excitation density $n_{\rm ex}$ defined in quasimomentum basis [Eqs. (S19)–(S21)] at intermediate times $t < T$. We use the notation K_q for the cumulants of the excitation density at $t < T$, and their definition coincides with κ_q at the final time $t = T$. The kink density cumulants in panels **a** and **b** are obtained from an MPS simulation.

V. CUMULANTS AS FUNCTIONS OF INSTANTANEOUS TIME

The main text discusses the defect statistics at the final time. For completeness, we investigate here how the defect density cumulants evolve in time, in particular the features that arise when crossing the phase transition. The defect density defined in the main text

$$\hat{n}_{\rm def} = \frac{1}{2N_e}\sum_{\langle i,j\rangle}(1 - \hat{Z}_i\hat{Z}_j) \tag{S34}$$

corresponds to kinks in the magnetization in position basis. These are topological excitations with respect to the final ferromagnetic ground state where all spins are aligned. The cumulants of the kink density are obtained as

$$\kappa_1 = \langle \hat{n}_{\rm def}\rangle, \quad \kappa_2 = N_e\left\langle (\hat{n}_{\rm def} - \langle \hat{n}_{\rm def}\rangle)^2\right\rangle, \quad \kappa_3 = N_e^2\left\langle (\hat{n}_{\rm def} - \langle \hat{n}_{\rm def}\rangle)^3\right\rangle. \tag{S35}$$

Evaluating them in the initial state $|+\rangle^{\otimes N} = \left[(|0\rangle + |1\rangle)/\sqrt{2}\right]^{\otimes N}$ gives $\kappa_1 = 1/2$, $\kappa_2 = 1/4$, and $\kappa_3 = 0$, and the final-state values are shown as functions of T in Fig. 3 of the main text.

Section IV, on the other hand, introduces the cumulants of the excitation density, obtained through the excitation probabilities p_k in quasimomentum basis in Eqs. (S19)–(S21). These are based on excitation probabilities with respect to the instantaneous ground state and coincide with the cumulants of the kink density at the final time $t = T$, where the ground state has all spins aligned. However, at $t < T$, the density of kinks differs from the density of excitations. In the following, we denote the cumulants of the excitation density at $t < T$ by K_q, with $q = 1, 2, 3$, corresponding to the mean, variance, and third central moment, respectively.

The cumulants of the kink density and excitation density are shown as a function of the unitless time t/T in Fig. S4 with and without CD. We focus here on the fast-quench regime with total time $T = 0.2/J$. For such short evolution times, the kink density cumulants remain close to their initial values when no CD is applied, as seen in Fig. S4a. In the presence of CD, the kink density and its variance are reduced, and the third central moment slightly increases to its final value shown in Fig. 3a in the main text. While the kink density cumulants do not have any distinguishing features at the phase transition point $t/T = 0.5$, the cumulants of the excitation density in Fig. S4a and Fig. S4b display a nonanalytic behavior. As the initial state is the ground state of H_i and there are no excitations, the cumulants K_q are zero at $t = 0$. The mean density of excitations K_1 grows monotonically, with an inflection point close to where the phase transition occurs. The variance K_2 increases up to the critical point and stays nearly constant at $t/T > 0.5$, with a discontinuous derivative at $t/T = 0.5$, while the third central moment K_3 has a peak at $t/T = 0.5$. The excitation statistics, therefore, show signatures of the phase transition that are not observed by measuring the kinks in the spin alignment. The same features occur in both finite-time annealing and counterdiabatic evolution, but K_1 and K_2 are suppressed by CD while K_3 increases slightly.

[S1] IBM Quantum, New fractional gates reduce circuit depth for utility-scale workloads, `https://www.ibm.com/quantum/blog/fractional-gates`, [Online: 17/01/25].

[S2] QPerfect, MimiQ Simulator, `https://www.qperfect.com/mimiq` (2023), version 1.2, Computer software.

[S3] J. Haegeman, C. Lubich, I. Oseledets, B. Vandereycken, and F. Verstraete, Phys. Rev. B **94**, 165116 (2016).

[S4] M. Fishman, S. R. White, and E. M. Stoudenmire, SciPost Phys. Codebases , 4 (2022).

[S5] P. W. Claeys, M. Pandey, D. Sels, and A. Polkovnikov, Phys. Rev. Lett. **123**, 090602 (2019).

[S6] Q. Xie, K. Seki, and S. Yunoki, Phys. Rev. B **106**, 155153 (2022).

[S7] A. G. Cadavid, A. Dalal, A. Simen, E. Solano, and N. N. Hegade, Bias-field digitized counterdiabatic quantum optimization (2024), arXiv:2405.13898 [quant-ph].

[S8] A. del Campo, Phys. Rev. Lett. **121**, 200601 (2018).

[S9] A. Grabarits, F. Balducci, and A. del Campo, Driving a quantum phase transition at arbitrary rate: Exact solution of the transverse-field ising model (2025), arXiv:2501.10478 [cond-mat.stat-mech].

[S10] J. Dziarmaga, Phys. Rev. Lett. **95**, 245701 (2005).

[S11] A. J. Berlinsky and A. B. Harris, The ising model: Exact solutions, in *Statistical Mechanics: An Introductory Graduate Course* (Springer International Publishing, Cham, 2019) pp. 441–476.

[S12] S. Suzuki, J. Inoue, and B. Chakrabarti, *Quantum Ising Phases and Transitions in Transverse Ising Models*, Lecture Notes in Physics (Springer, 2012).

[S13] F. J. Gómez-Ruiz, J. J. Mayo, and A. del Campo, Phys. Rev. Lett. **124**, 240602 (2020).